Thin Solid Films 735 (2021) 138862

Contents lists available at ScienceDirect

Thin Solid Films

journal homepage: www.elsevier.com/locate/tsf

Unexpected precipitates in conjunction with layer-by-layer growth in Mn-enriched $La_{2/3}Sr_{1/3}MnO_3$ thin films

Alexandra Steffen [a,b], Artur Glavic [*,c], Thomas Gutberlet [d], Haile Ambaye [b], Jürgen Schubert [e,f], Stephan Geprägs [g], Juri Barthel [h], Stefan Mattauch [a], Willi Zander [e,f], Maximilian Kruth [h], Patrick Schöffmann [a], Sabine Pütter [a], Thomas Brückel [d]

[a] Forschungszentrum Jülich GmbH, Jülich Centre for Neutron Science (JCNS) at Heinz Maier-Leibnitz Zentrum (MLZ), 85748 Garching, Germany
[b] Neutron Sciences Directorate, Oak Ridge National Laboratory, Oak Ridge 37831, Tennessee, USA
[c] Laboratory for Neutron and Muon Instrumentation, Paul Scherrer Institut, 5232 Villingen PSI, Switzerland
[d] Forschungszentrum Jülich GmbH, JCNS-2, 52425 Jülich, Germany
[e] Forschungszentrum Jülich GmbH, PGI-9, 52425 Jülich, Germany
[f] JARAFIT, Forschungszentrum Jülich GmbH, 52425 Jülich, Germany
[g] Walther-Meißner-Institut, Bayerische Akademie der Wissenschaften, 85748 Garching, Germany
[h] Forschungszentrum Jülich GmbH, ER-C-2, 52425 Jülich, Germany

ARTICLE INFO

Keywords:
Thin film
Nanoscale structure
Oxides
Precipitation
Lanthanum strontium manganate
Molecular beam epitaxy
Polarized neutron reflectometry

ABSTRACT

In recent years, layer-by-layer heteroepitaxy has become a versatile tool for depositing novel materials not accessible in bulk form. While it is possible to control the mono layer sequence on an atomic scale with the help of sophisticated analysis techniques, not all important features of the thin film growth are detectable. We report on a detailed analysis of layer-by-layer deposited Mn-enriched $La_{2/3}Sr_{1/3}MnO_3$ thin films using various, complementary experimental techniques. Our results show that, contrary to the expectations from the growth parameters and initial characterization, the films did not grow as atomic planes but segregated into layers of $La_{2/3}Sr_{1/3}MnO_3$ with additional embedded precipitant crystals. We attribute this separation to a Volmer-Weber island-like growth of Mn_3O_4 crystals within layers of $La_{2/3}Sr_{1/3}MnO_3$ due to increased surface tension inhibiting La and Sr oxides from sticking to nucleated Mn_3O_4 surfaces during the growth at high temperatures.

1. Introduction

Advances in synthesis techniques enabled the growth of atomically-controlled heterostructures. In such multilayer films, the chemical composition parallel to the substrate surface (in-plane) is constant, but varies perpendicular to the surface (out-of-plane, here +z), allowing to create materials with new physical properties. As an example, utilizing films with graded modulations of the nominal total layer stoichiometry, Kirby et al. [1] showed that a smoothly graded 100 nm $Ni_{x(z)}Cu_{1-x(z)}$ alloy film exhibits a ferromagnetic phase transition similar to a continuum of uncoupled ferromagnetic layers with distinct Curie temperatures.

As many groups report about the successful growth of such complex structures, verifying that by different methods, it can be tempting to assume that the desired structure was realized when only a single analytic method is applied to support that assumption. Using a limited number of experimental techniques, as often done due to time and access constraints, one can only investigate certain aspects of the deposited structure, which can lead to false conclusions. The major characterization technique applied to control the film growth is reflection high-energy electron diffraction (RHEED), since it can be performed in-situ during the deposition. It is non-destructive, and doesn't require additional sample preparation as other techniques. Only the first few atomic layers are contributing to the observed RHEED pattern, which makes this method extremely surface-sensitive. It offers a fast method to distinguish between an amorphous sample (no pattern), a polycrystalline one (ring structure pattern), and a single crystalline film (distinct spots in observed pattern) [2]. If the RHEED pattern is observed during growth, different growth modes [3] can be distinguished from each other due to the influence of nucleating particles onto the pattern of a perfect surface [4]. Oscillations of the RHEED intensity of the specular spot are observed during crystalline film growth, where each oscillation

* Corresponding author.
E-mail address: artur.glavic@psi.ch (A. Glavic).

https://doi.org/10.1016/j.tsf.2021.138862
Received 5 January 2021; Received in revised form 26 July 2021; Accepted 26 July 2021
Available online 1 August 2021

period corresponds to the growth of one atomic unit cell [5].

$La_{2/3}Sr_{1/3}MnO_3$ (LSMO) is showing a fascinating variety of magnetic effects caused by the interaction of spin, charge, orbital, and lattice degrees of freedom [6,7]. Bulk LSMO with x=0.3 is ferromagnetic below 370 K. Utilizing RHEED-based thin film preparation techniques, different individual layer thicknesses of the $[(LaMnO_3)_{2n}/(SrMnO_3)_n]$ system can be produced, where the total film stoichiometry is still that of LSMO [8]. In this $[(LaMnO_3)_{2n}/(SrMnO_3)_n]$ system, the individual films can be magnetically tuned ranging from anti-ferromagnetic to ferromagnetic behavior, triggered by the number of mono layers (ML) n. In this study we will focus on a 25 nm thin $(La_{2/3}Sr_{1/3}O)/(MnO_2)_{n(z)}$ layer system based on $(La_{2/3}Sr_{1/3}O)/(MnO_2)$ with additional MnO_2 MLs, inserted at different vertical positions, expected to form a Mn gradient structure by local incorporation of these MnO_2 MLs similar to a Ruddlesden-Popper series. This way we would not only vary the Mn magnetic moment and coupling by changing the oxidation state but, instead, introduce layers with different Mn-O coordination and thus coupling symmetry aligned with the growth direction. Similar growths have been carried out successfully on $SrTiO_3$ before [9,10] as well as on $Cu(In,Ga)Se_2$[11]. If realized correctly, these samples would be useful to study how the magnetic profile follows the nuclear structure and how neighboring atoms are magnetized, respectively. We find, however, using several complementary experimental techniques that the actual grown films do not show the expected structure. During the film growth only LSMO forms closed epitaxial layers while the excess Mn clusters together in MnO_x precipitants.

2. Methods

2.1. Film deposition

LSMO films were deposited onto (001) oriented $SrTiO_3$ (STO) substrates (Crystec GmbH) via molecular beam epitaxy (MBE) using a DCA M600 system. The substrates were cleaned via heating up to 1000°C in Ultra High Vacuum and subsequently in an oxygen plasma in order to remove carbon-based contamination and to re-saturate the oxygen concentration. The substrate temperature during growth was 900°C to minimize the zig-zag shaped [12] or undulating interface [13] of the individual Mn_3O_4/ LSMO interfaces. For all growth protocols discussed here, two samples were grown at the same time to create twin samples with different size, a 5mm x 5mm sample for Superconducting QUantum Interference Device (SQUID) measurements and a 10mm x 10mm sample for the Polarized Neutron Reflectometry (PNR) measurements. La, Sr and Mn were evaporated at temperatures around 1500°C (La), 500°C (Sr) and 850°C (Mn), leading to growth rates of one unit cell per approx. 2 minutes. The MBE base pressure with all effusion cells at room temperatures was 10^{-8} Pa. At targeted evaporation temperatures, the MBE pressure was 10^{-6} Pa. The films were grown in oxygen plasma as oxygen supply with a flux of 0.22 sccm leading to a MBE growth pressure of 10^{-3} Pa. The deposition rates were calibrated via a Quartz Crystal Microbalance (QCM) for one-week pre-growth to guarantee a stable element flux during the sample growth. The sample surface was monitored during growth via time-resolved RHEED. The depth information like in X-Ray diffraction (XRD) is lost due to multiple electron scattering; on the other hand, the bulk is not contributing to the RHEED pattern, only the film surface is accessible.

Thin LSMO films were grown in shuttered deposition: either the La and Sr shutters or the Mn shutter were opened with an opening interval length t corresponding to the deposition time of a single ML. By this method the LSMO perovskite cube is sliced into an (La/Sr)O ML and a MnO_2 ML. It was intended to introduce additional MnO_2 MLs via additional Mn shutter opening times, leading in total to an over-doped Mn concentration. The MnO_2 excess was deposited at different times during deposition, namely a) constant during growth, b) at the end of the deposition process, c) at start and end of the deposition process, and d) in the middle of the deposition process. If the samples crystallized in the same chronological timeline as the material was offered, this should lead to a Mn excess profile with a constant Mn concentration in case a), b) more additional Mn towards the surface, c) more Mn at top and bottom of the total film structure, and d) more Mn in the middle section of the film structure. Samples grown with these deposition schemes were studied in detail with particular focus on the realized vertical Mn profiles.

2.2. SQUID measurements

Magnetic characterization to measure the Curie temperature via magnetic field vs. temperature measurements and the magnetic hysteresis via magnetic field vs. magnetic moment measurements was carried out on a SQUID magnetometer Quantum Design MPMS XL-7.

2.3. RHEED

RHEED was performed at 15 keV and 1.5 A. The STO substrate was aligned in [100] along the RHEED beam direction with an uncertainty of 0.5°. To observe the sample growth in-situ, the RHEED intensity of the specular spot was monitored.

2.4. X-ray diffraction and reflectivity

X-Ray reflectivity (XRR) measurements were performed to determine the total film thickness, the roughness and the sample composition via electron density determination. Via XRD the crystalline layer thickness and out-of-plane lattice parameter was determined. XRR and XRD measurements were performed on Bruker D8 Discover machines in $\omega - 2\Theta$ geometry using a Cu-k_α tube source with Göbel mirror monochromator.

2.5. AFM

For real-space surface morphology determination, Atomic Force Microscopy (AFM) was performed on an Agilent 5500 SPM.

2.6. X-ray spectroscopy and transmission electron microscopy

In preparation for the energy dispersive X-ray spectroscopy (EDX) and the transmission electron microscopy (TEM), thin cross-section lamellae were extracted from a selected sample area using an FEI Helios Nanolab 400 focused ion beam (FIB) [14]. The orientation of the lamella was chosen such that a <001> zone axis of the film material is along the thin lamella axis. The extracted lamellae were thinned and cleaned further by low energy Ar-ion milling with a Baltec RES 120 to a thickness well below 50 nm. The EDX measurements to determine the local stoichiometry was performed with an FEI Tecnai G2 F20 transmission electron microscope operated at 200 kV accelerating voltage [15].

2.7. High-resolution electron microscopy

High-resolution scanning transmission electron microscopy (STEM) was performed with a probe CS-corrected FEI Titan 80-300 instrument operated at 300 kV accelerating voltage [16]. High-angle annular dark field (HAADF) images were recorded providing contrast proportional to the atomic number. In combination with an electron probe size of less than 0.1 nm this Z-contrast imaging technique allows us to distinguish the columns containing A-site atoms (La, Sr) from the columns containing the Mn atoms, when the film structure is viewed along an <001> zone axis.

2.8. Neutron reflectometry

Polarized Neutron Reflectometry (PNR) to determine the chemical

and magnetic vertical film profile was measured at MARIA@MLZ [17] and the Magnetism Reflectometer@SNS [18]. The measurements were performed at 5 K and 1.2 T and the non-spin-flip channels were measured up to Q=0.15 $Å^{-1}$.

3. Results and discussion

For shuttered growth, the (La/Sr)O MLs are deposited while the Mn effusion cell is closed and vice versa MnO_2 MLs are deposited with closed La/Sr cells. In case of successful growth of a (La/Sr)O ML, the specular RHEED intensity is supposed to drop, while for the subsequent MnO_2 ML, the intensity should rise again, leading to an oscillation of the RHEED intensity for growth of multiple unit cells via the shuttered growth technique [5]. In Fig. 1 to 3, the RHEED intensities vs. time during growth are displayed. The effusion cell shutter sequences are marked with green and purple bars indicating open La/Sr and MnO_2 shutters, respectively.

The additional Mn in LSMO is deposited by opening the Mn shutter for double the amount of time that is needed to grow a single layer with height of 1 unit cell MnO_2. Then n amounts of LSMO unit cells are deposited in shuttered growth mode, until the total desired stoichiometry of $(LS)_n(M)_{n+1}O$ is reached. For all samples with additional Mn deposited at different times during the growth, the observed RHEED intensity oscillations are in accordance with the opening and closing intervals of the effusion cell shutters (green: LS-shutter open, intensity increases, and purple: Mn-shutter open, intensity decreases). This indicates that the evaporated material reaches the substrate surface in the applied deposition sequence, realized via opening times of the effusion cell shutters, indicating a "MBE recipe-based" vertical sample stoichiometry. Moreover, the additional insertion of the MnO_2 layers changes the surface roughness drastically which is expressed by higher oscillation of the amplitude of the intensity.

Via out-of-plane XRD scans, the expected STO substrate and LSMO film peaks were observed without any additional reflections (Fig. 4). The out-of-plane lattice parameters of the films are in the range of 3.85 Å to 3.87 Å. Assuming that this parameter is mainly given by the LSMO contribution, these parameters are in good agreement with ref. [19] and could be interpreted as a hint that the additional Mn crystallized at the desired positions without introducing a new crystal structure, namely via clustering as phase-separated MnO_2 particles inside the LSMO material.

Via AFM, the surface was investigated (Fig. 5). The images show atomically flat terraces with additional hills of height one order of magnitude bigger than the atomic steps.

X-ray reflectivity data were analyzed to determine the total (LS) xMyO film thickness due to the large electron density contrast of LSMO and STO for X-rays and the surface roughness due to the large accessible Q range. PNR data were evaluated regarding the chemical (stoichiometric) vertical composition and the magnetic profile. The neutron data at two temperatures and the x-ray data were co-refined to the same structural model using the GenX software package [20].

In Fig. 6 and 7 a, the Nuclear Scattering Length Density (NSLD) model is based on assumed chemical composition of the film along the growth direction, the "MBE recipe based fit". A surface roughness region is also included. The Magnetic Scattering Length Density (MSLD) in each

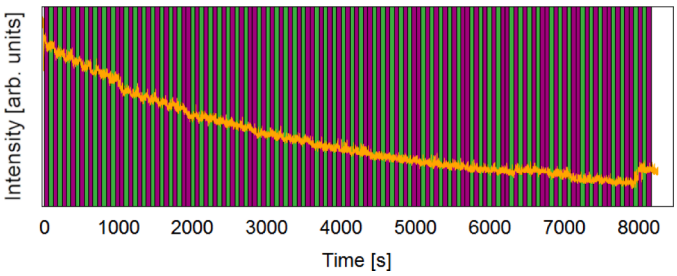

Fig. 2. RHEED intensity vs. deposition time; recorded during the deposition of sample 224, a LSMO thin film with more Mn deposited towards the end of the film deposition.

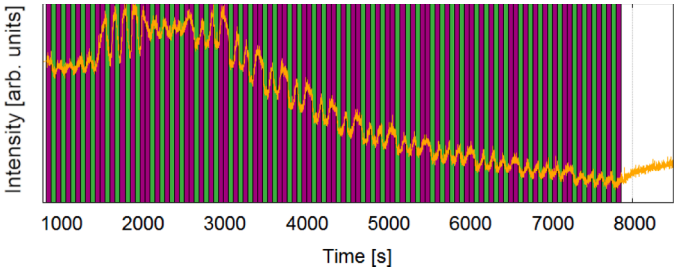

Fig. 3. RHEED intensity vs. deposition time; recorded during the deposition of sample 233, a LSMO thin films with additional Mn deposited in the middle of film deposition.

Table 1
List of Samples

	Sample description	scheme
Sample 230	Increased Mn deposited at beginning and end of growth	c)
Sample 224	Increased Mn deposited towards the end of growth	b)
Sample 233	Increased Mn deposited in the middle of the growth	d)
Subdivision a/b	Large/small sample deposited at the same time	

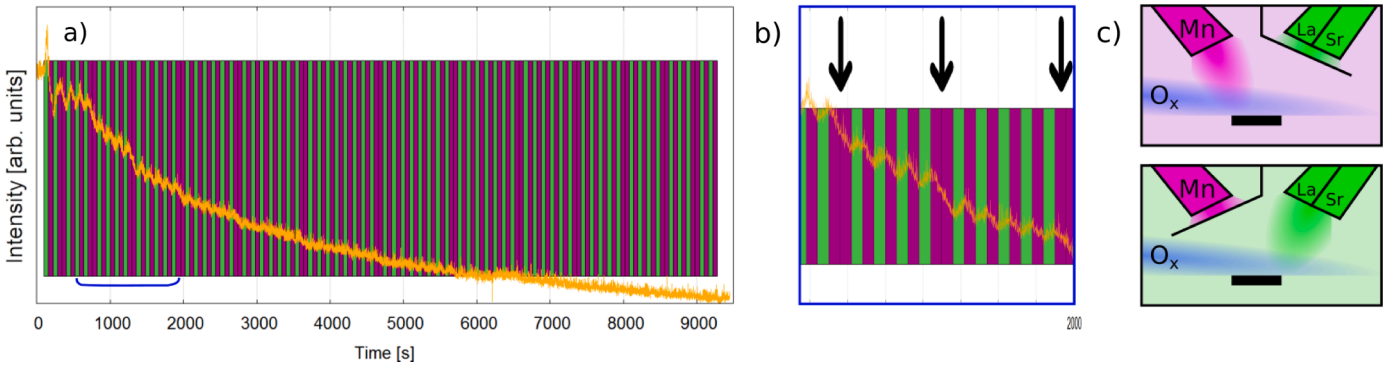

Fig. 1. RHEED intensity vs. deposition time (a) and zoom to start of deposition (b); recorded during deposition of sample 230 with higher Mn density deposited at the start and the end of the film deposition. The green (purple) bars indicate the time intervals when the La/Sr (Mn) shutter is open, this is illustrated in the sketches (c). In case of the deposition of an additional MnO_2 ML, the width of the purple stripe is doubled (arrows) and therefore easily visible in the overview image (left). There are more additional purple stripes towards the start and the end of the film growth, leading to a nominal Mn stoichiometric gradient with more Mn on top and bottom of the film than in the middle.

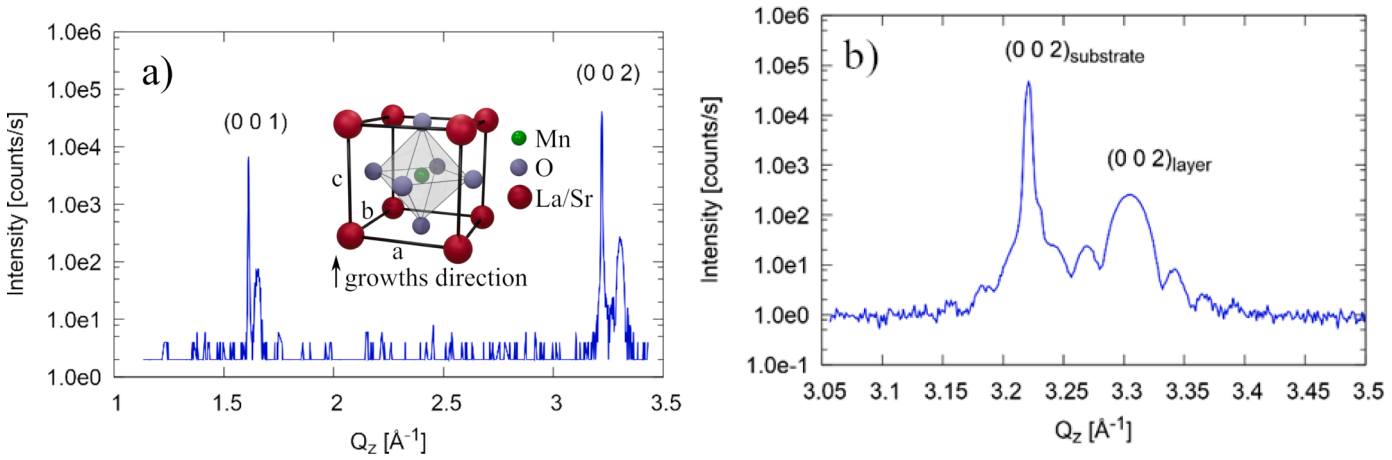

Fig. 4. Representative out-of-plane XRD scan, overview area (a) and detail around (0 0 2) (b), showing only STO substrate peaks (sharp peaks of high intensity), LSMO film peaks (wider peaks with lower intensity due to limited film thickness) and crystalline layer thickness fringes. Inset shows the crystallographic unit cell of LSMO.

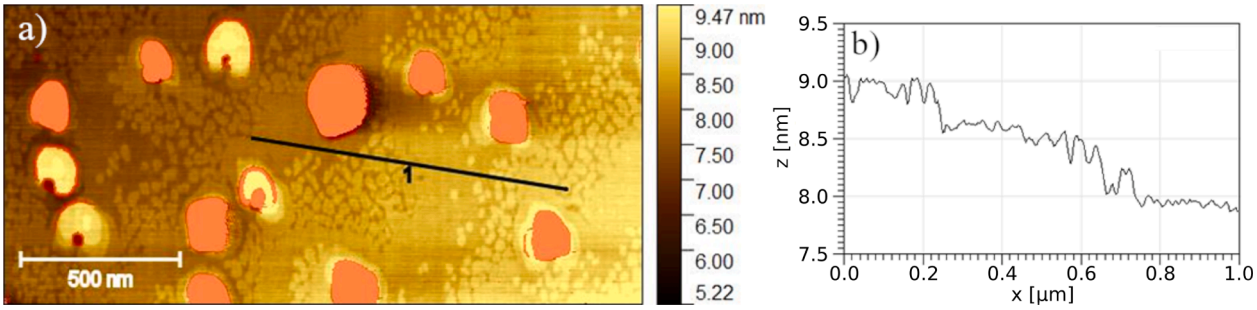

Fig. 5. AFM height image showing atomically flat terraces and visible precipitates. The profile (b) represents a cut along the line indicated in the overview image (a). Root mean squared roughness of 0.67 nm without masked precipitates, 9.69 nm including the precipitates.

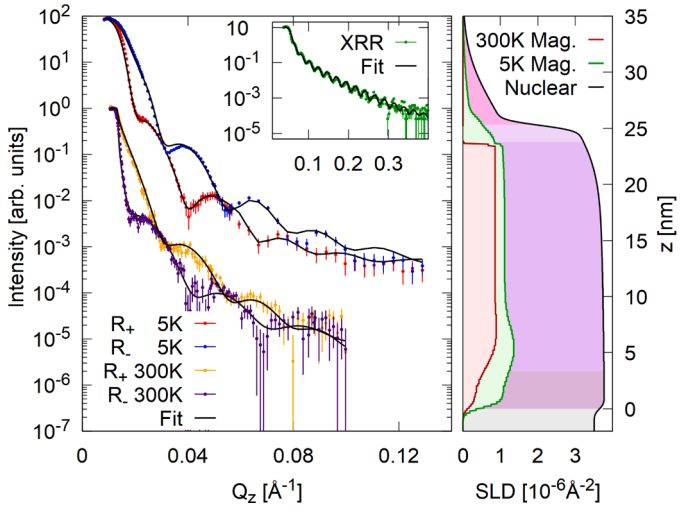

Fig. 6. Sample 224; XRR and PNR measurements and simulations to investigate the film morphology. Left: PNR measurements at 5 K and 300 K with R_+ and R_- indicating the different polarization of the neutrons. The inset shows the XRR measurement. Right: The used magnetic (MSLD) and nuclear (NSLD) scattering length densities. For visibility, the 5 K PNR measurements were shifted in intensity. The different purple colors used for the NSLD represent the slabs needed to model the recipe-based stoichiometry profile in the software.

model slap is not constrained while optimizing the figure of merit (FOM). In Fig. 7b, the measurements of Fig. 7a were fitted, using a model assuming embedded surface particles via a reduced density towards the sample surface. As can be seen, the model in Fig. 7b much better describes the measured data and is more physical. The alternative model based on the expected structure is not only a much worse fit to the PNR at 300 K but has approached a non-physical behavior where there is a magnetic dead layer near the substrate. The combined fitting of PNR and XRR data showed the nuclear structure inside the thin film samples being different from the one expected from the intended growth of MnOx excess regions (Fig. 7a using the MBE recipe, Fig. 7b using the surface particle model). In the scattering length density (SLD) profile of the PNR data, a Mn excess is simulated via a reduced SLD value due to the negative scattering length of Mn. Here, all samples had a typical LSMO SLD at the substrate interface and a reduced SLD at the surface, which can be caused either by a Mn excess or a reduced layer density, e. g. by a porous and rough surface. The data revealed pure LSMO at the substrate interface with a reduced SLD towards the surface for all investigated samples.

STEM imaging was performed on a cross section area with length of 1.6 μm. The images show large areas of a homogeneous film with identical thickness and in addition the existence of precipitates. The surface of these precipitates was visible in surface SEM images taken during the FIB preparation process, too. With respect to the MBE recipe for the effusion cell shutters, taken at the homogeneous film area in Fig. 8, 14 additional MnO_x MLs are expected, each contributing a monolayer thick rock salt structure, which should be visible in the HAADF STEM images. However, with the exception of the precipitates which couldn't be clearly identified, an otherwise perfectly coherent

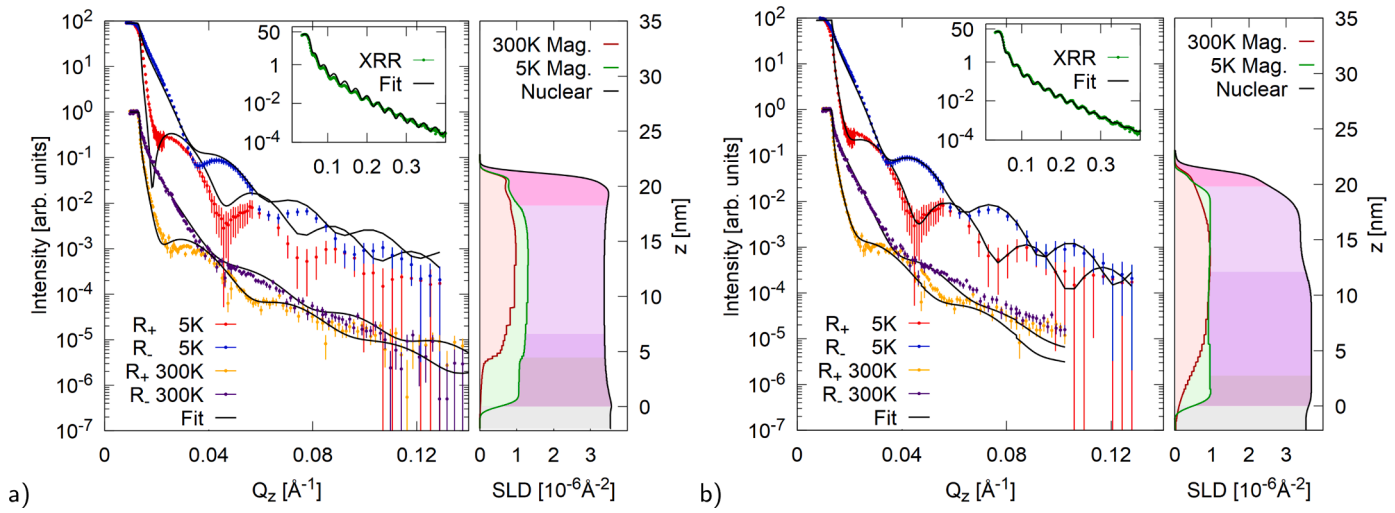

Fig. 7. Sample 233; XRR and PNR measurements and simulations to investigate the film morphology. Left: PNR measurements at 5 K and 300 K with R_+ and R_- indicating the different polarization of the neutrons. The inset shows the XRR measurement. Right: The used magnetic (MSLD) and nuclear (NSLD) scattering length densities. For visibility, the 5 K PNR measurements were shifted in intensity. The different purple colors used for the NSLD represent the slabs needed to model the recipe-based stoichiometry profile in the software. For sample 233a the two different models (a) and (b) represent an expected and fitted structural profile, where the latter has 30% better FOM.

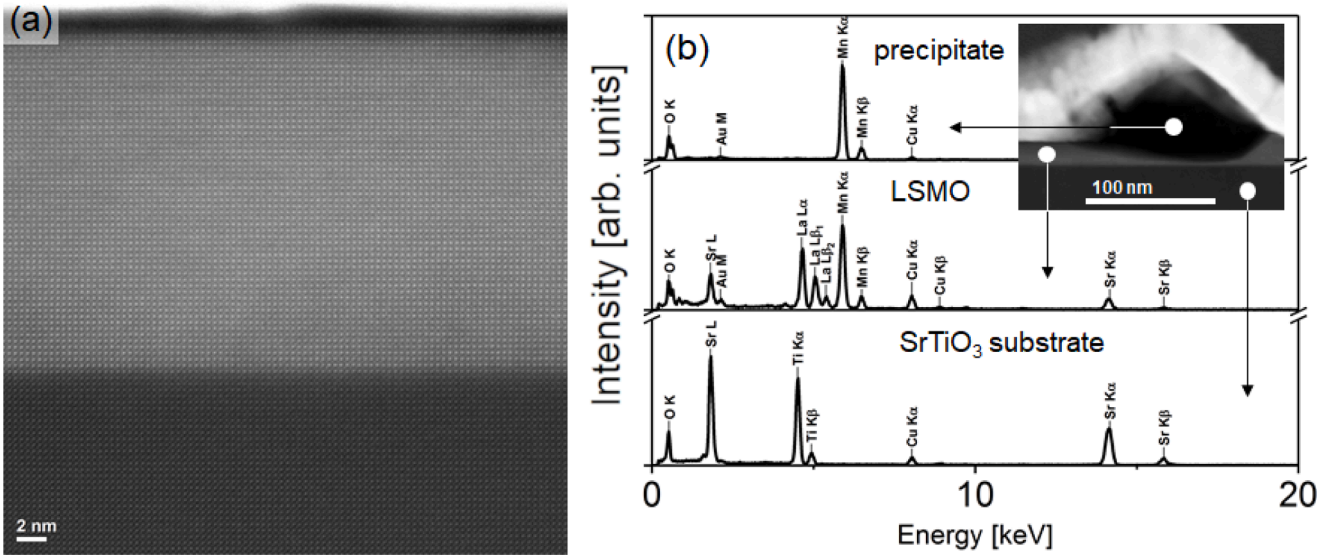

Fig. 8. Cross-section images of the sample 230 with more Mn deposited at the start and at the end of the film deposition: a) High resolution STEM image: Pure perovskite structure, b) EDX spectra recorded from substrate, film and precipitate areas. Locations of EDX measurements can be seen in the inset image showing the area around a very large precipitate. Additional Cu signal in the EDX spectra originates from the sample holder material.

perovskite structure is observed over the whole investigated cross-section area. Inside the well-ordered film, there is no sign of any additional rock salt structure, and neither vertical stoichiometric gradients nor vertical MnO_X structures are observed. Between substrate and film, there is a sharp interface as well as a sharp surface on top of the sample, which shows no sign of significant surface roughness. The EDX measurements performed on the same sample area are consistent with the observations made in the high-resolution STEM images and agree with the stoichiometry of LSMO. The investigated precipitates contain Mn and O.

SQUID magnetization vs. temperature measurements revealed three transition temperatures: The LSMO Curie temperature above 300 K, the cubic-to-tetragonal transition of the STO substrate around 105 K, and an additional kink below 50 K (Fig. 9a). As this feature is near the paramagnetic-to-antiferromagnetic oxygen transition temperature [21, 22], which could be the result of frozen oxygen on the sample surface, we have analyzed the magnetic hysteresis at different temperatures (Fig. 9b,c) by fitting it with a simple hysteresis loop model that includes only three free parameters, saturation magnetization M_{sat}, coercive field H_c and a magnetic softness parameter defining the curvature of the function. We find good agreement with the data and a model of two hysteresis, which points to the presence of to ferro- or ferrimagnetic phases in the sample. The contribution with the larger coercive field has about 10% of the magnetization in the sample at 5 K and vanishes at round 50 K, consistent with the temperature dependent data.

With respect to the EDX measurements, it is known that there is a MnO_y excess with unknown oxygen content y. In the family of manganese oxides, Mn_3O_4 has a phase transition from paramagnetic to ferrimagnetic below 41-43 K [23]. Therefore, the kink below 50 K is likely an indicator for the presence of Mn_3O_4. The total moment found for the

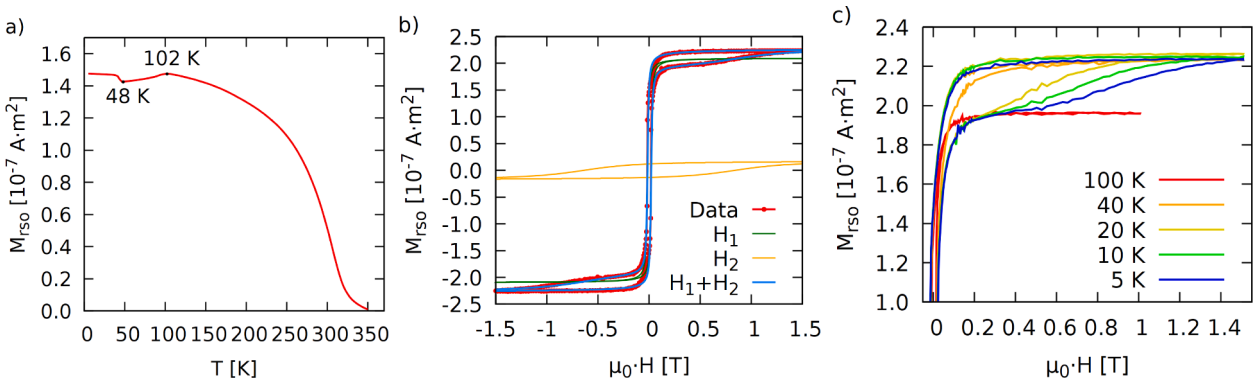

Fig. 9. SQUID measurements of a sample with more Mn deposited at the start and the end of the film deposition: a) Field-cooled magnetization versus temperature measured at 10 mT, b) magnetic hysteresis loop at 5 K, fitted with the sum (H1+H2) of 2 independent loops (H1, H2), and c) zoom to one side of hysteresis measured at different temperatures.

second contribution of the hysteresis would not correspond to an antiferromagnetic order and the amount is consistent with expectations for precipitates formed from the additional manganese of the deposition. After removing the Mn needed to form the LSMO complete film, 30% of excess Mn is available to form precipitates. If all Mn is used to form Mn_3O_4 the effective magnetic moment per atom would be around 0.6 μ_B [24], 1/3 of that expected for LSMO thin films, which explains a 10% additional magnetic moment that was observed. The coercive field of around 300 mT @ 5 K also supports this hypothesis.

Even though the thin film material was deposited in a sequence to create graded Mn(z) profiles, the final film composition turned out to be pure LSMO with MnOx precipitates at the surface. Two details are interesting; first, that the material crystallized in such a different way, and second, which techniques are capable to detect a result differing so much from the expected outcome.

Other groups studied $LaMnO_3$ and LSMO single crystals, grown via molten rod methods, e.g. floating zone or Czochralski processes. There, the liquid reacts with the feedrod, and the growth is dominated by the rejection of dopant atoms by the crystal as it forms; the pure, single crystal crystallizes, and inside the liquid the dopant element concentration increases [25]. In addition, for single crystals it was found that during growth Mn evaporates from the melt for $LaMnO_3$ [26]. At a growth temperature of 1000°C (1273 K), for single crystals in the pseudo-binary La_2O_3-Mn_3O_4 phase diagram the existence of the perovskite $LaMnO_3$ plus (tetragonal) Mn_3O_4 phase for Mn excess is observed [27]. Apparently, similar processes took place in the here observed thin film growth. The films were deposited with 0.3 nm/minute, which is plenty of time for a diffusion process of atoms on a terrace or to a lower terrace [28]. Here, LSMO still grows epitaxially, but the additional MnO diffuses towards other MnO.

For thin films, Ishii et al. [29] pointed out that already during the film deposition, a surface in a non-equilibrium state can give rise to adsorption, surface diffusion, and dissociation processes before the incoming oxidized La, Sr and Mn crystallize as layer or nucleate as precipitate. In case of small deviations from ideal stoichiometry, they observed a homogeneous defect particle distribution on the sample with a maximum particle distance for samples grown at the maximum investigated temperature of 900°C [29].

The here used growth parameters were optimized for co-deposition, where La, Sr, and Mn are deposited simultaneously. Due to the effusion cell-based deposition method, calibrated via quartz crystal microbalance (QCM), the stoichiometric error bar of this growth method is in general less than 2% [5]. But while for co-deposition homogeneous films can be achieved by letting the single atoms diffuse into the targeted position, in shuttered deposition mode it is crucial that the deposited atoms stick and form a smooth coherent ML. The atoms forming this single ML need enough energy to crystallize as part of the underlying perovskite lattice instead of forming an amorphous film. In addition, the new film is not supposed to have enough energy to cluster with itself rather than with the underlying material [4].

Since Mn_3O_4 and LSMO are chemically compatible [30], the LSMO/MO multilayers and gradient structures were grown at high temperatures to achieve high defect distances. Small amounts of solid state diffusion might occur, but the number of crystallographic defects was supposed to be low enough to create a sufficient sample quality and the LSMO structure should profit from the high temperatures, showing epitaxial growth with low out-of-plane lattice parameters and a high Curie temperature. By using relatively high growth temperatures, the areas of pure LSMO stoichiometry turned out to be enlarged (Fig. 8).

Still, the final films have a drastically different Mn(z) profile. Obviously, the used growth conditions supply La, Sr, and Mn with enough energy to rearrange and crystallize first in the stable $(LS)_1M_1O$ composition. There are no traces of additional Mn at the LSMO/STO interface. The additional MnO is segregated (Fig. 10) and finally clusters towards the surface, minimizing the well-defined interface towards the LSMO by forming spheres or ellipsoids, and partially crystallizing above the LSMO film height (Fig. 10). Therefore, the actual crystallization process is far more relevant than the used sequence of the deposited material. At low substrate temperatures, the stacking is purely given by the deposition sequence, but epitaxial growth of oxides is not achieved, the film roughness is high, and the film density might be low. At very high deposition temperatures, equilibrium growth like observed in single crystals dominates the growth.

The RHEED specular intensity exhibits a single oscillation for a completed LSMO ML as shown here. For one additional MnO ML the intensity drops further, afterwards LSO is again offered - leading to an increase in intensity, followed by a MnO ML, again decreasing the intensity. This can be mistaken as the RHEED intensity oscillations document that targeted growth of the Mn-graded structures. Instead, RHEED revealed the crystallized unit cells, further intensity decreases due to a higher amount of non-ordered MnO precipitates at the surface; a decrease of intensity is first of all related to an increase of surface roughness. This behavior does not necessarily indicate the expected structure of the sample. On the other hand, if the total numbers of RHEED oscillations is compared with the crystallized LSMO unit cells of

Fig. 10. Representation of Mn content within the film. The final sample composition is pure LSMO with encapsulated MnOx and a sharp interface (left), which differs a lot from the targeted sample composition which should produce a Mn(z) profile (right), here with a higher Mn concentration at the top and the bottom of the film as was used in sample 230.

the flat LSMO film investigated via TEM, these numbers are identical, showing that RHEED observed the correct amount of the crystallized main structure, LSMO.

SQUID measurements as macroscopic methods revealed the Curie temperature of the LSMO parts, an important criterion for the film quality. But these measurements cannot be used to distinguish if Mn_3O_4 clusters or additional Mn_3O_4 layers contribute to the second kink of the measurements.

With AFM and SEM, probing a local part of the samples, a part of the surface shape can be detected, and the distinction can be made if a sample is atomically flat (still showing the atomic-high steps of the substrate) or rough (not showing these steps). The strived Mn(z) profile cannot be detected due to its z dependency. TEM cross-section imaging with a spatial resolution around 0.1 nm is sufficient to determine a local Mn(z) profile despite the averaging over a typical sample thickness of about 20 nm. In the present case, this technique provides a clear evidence for the absence of the desired Mn(z) profile.

XRR and PNR as scattering methods provide averaged information of the whole sample; in particular, they can be utilized to determine whether the composition profile deviates or agrees with the targeted profile without damaging the sample. In specular reflectivity geometry, the out-of-plane information is depth-resolved while the in-plane information is averaged. To show the influence of different local features in a thin film sample, sketches are given in Fig. 11. The scattering length density measured in reflectivity is the integrated density of the scattering lengths of all atom in the plane of the sample.

In Fig. 11a, a perfect film is displayed. The interface film/vacuum is flat; the projection on z shows a clear step function. In Fig. 11b, a second layer with a smaller SLD (any manganese oxide (MO)) is on top of the original layer, leading to a second step in SLD. In Fig. 11c and 11 d, the top and bottom layer show different kinds of uncorrelated roughness. Fig. 11c shows a high surface roughness or island growth of the same material and in Fig. 11d droplets of the MO material are embedded in the film. While the differences between model in Fig. 10 can be distinguished easily by reflectometry the small changes from 11 c to 11 d may not be obvious, especially when the in-plane density of the surface structure is unknown.

For Neutron Reflectivity the difference between MnO and LSO is by far bigger than for X-rays due to the negative scattering length of Mn. While the X-ray data can be fitted with a single, rough LSMO layer with constant stoichiometry, the neutron data clearly point out the additional MnOx at the surface (see Fig. 7a and b). In addition, the depth-resolved magnetic profile revealed via PNR emphasized the LSMO area.

4. Conclusion

To realize a global-defined stoichiometry, various options exist via different growth modes of local structure e.g. layer by layer growth, layer plus island or isolated island growth or different compositions as homogeneous layers, precipitates, material segregation or defects. There are several potential sources for a deviation of the growth performance from the expected outcome. Parameters like substrate quality, stability of the effusion cell rates, chamber pressure during growth, substrate temperature during growth, and the cooling down procedure impact the growth. LSMO films prefer single-phase crystallization. In terms of additional Mn_3O_4 layers inside this LSMO film, growth conditions can lead to phase separation instead of a multilayer structure where additional Mn_3O_4 diffuses and clusters in nonhomogeneous precipitates with observed diameter size of 50 Å to 500 Å and distance of 500 Å to 2500 Å. This is quite different from previous findings for spinel-perovskite phase separation, a combination of well related oxides driven by elastic interaction, where an epitaxial growth of both phases in a self-assembled pillar structure is possible [31–33] or on more complex oxide systems that can form very inhomogeneous inclusions [34]. The final film material is not only dependent on deposited material or deposition sequence, but on a complex growth process. In the present work, the substrate temperature during growth was relatively high (900°C instead of 650°C to 750°C used in literature), encouraging the evaporated material to recombine before local crystallization takes place.

The identification of the proper growth conditions requires the application and combination of several complementary and elaborate structure characterization techniques. Different characterization methods have different sensitivity to probe the resulting film structure or precipitate formation. Standard in-house methods (RHEED, XRR, XRD) provide incomplete information on the successful deposition of single atomic layer variations in thin films. While the height of flat areas between precipitates corresponds to the observed RHEED oscillations, the RHEED intensity oscillations do not give information about purity/mono-phase of the film or depth-resolved local stoichiometry. AFM and SEM measurements of the surface morphology must agree with via RHEED, XRD, XRR predicted sample surface. The structural profile inside LSMO was revealed via PNR and TEM which includes insight regarding the crystallization process.

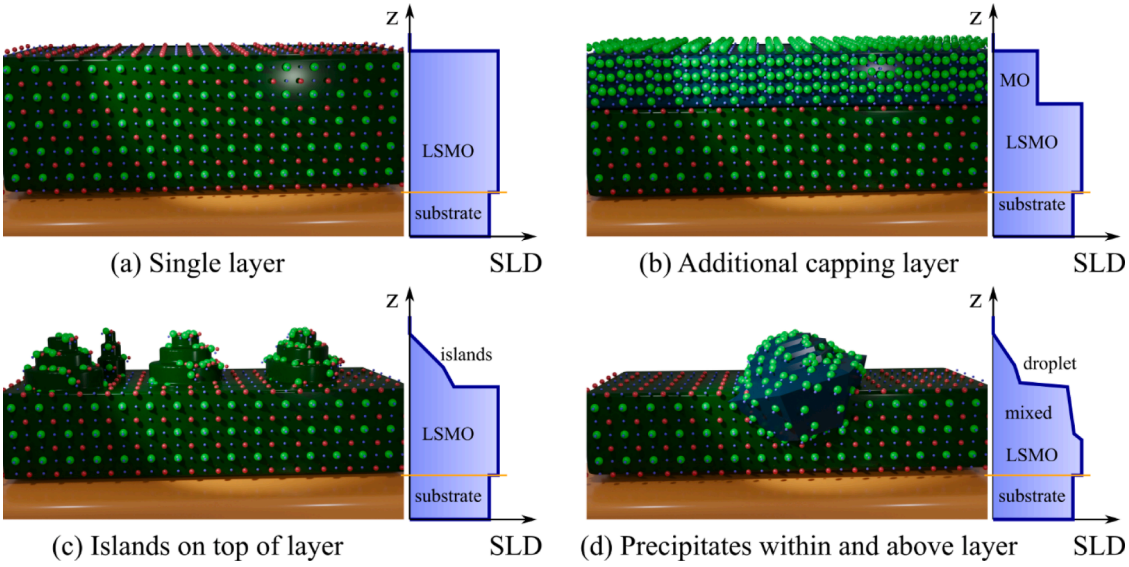

Fig. 11. Visualization of different sample models and the associated neutron scattering length density (SLD) that results from integrating in the sample plane. In particular model (d) with precipitates illustrates how the complex SLD profile of the used model arises from the structure.

CRediT authorship contribution statement

Alexandra Steffen: Conceptualization, Methodology, Software, Validation, Formal analysis, Investigation, Resources, Data curation, Writing – original draft, Visualization, Supervision, Project administration, Funding acquisition. **Artur Glavic:** Project administration, Validation, Investigation, Data curation, Writing – review & editing, Visualization. **Thomas Gutberlet:** Writing – review & editing. **Haile Ambaye:** Resources. **Jürgen Schubert:** Investigation, Resources. **Stephan Geprägs:** Resources. **Juri Barthel:** Software, Investigation, Resources, Visualization. **Stefan Mattauch:** Investigation, Resources, Data curation. **Willi Zander:** Resources. **Maximilian Kruth:** Investigation, Resources. **Patrick Schöffmann:** Validation, Investigation. **Sabine Pütter:** Validation, Investigation, Resources. **Thomas Brückel:** Validation, Resources, Writing – review & editing, Supervision, Funding acquisition.

Declaration of Competing Interest

The authors declare that they have no known competing financial interests or personal relationships that could have appeared to influence the work reported in this paper.

Acknowledgment

The authors thank Olaf Holderer for initial ideas and scientific input. The authors gratefully acknowledge Harald Schneider's instrumental support at MLZ regarding the Oxide MBE and the polarized neutron reflectometers TREFF and MARIA. The authors further like to thank Alexander Weber for his work on TREFF data reduction and initial support of PNR data interpretation. Research at Oak Ridge National Laboratory's Spallation Neutron Source was sponsored by the Scientific User Facilities Division, Office of Basic Energy Sciences, and U.S. Department of Energy. ORNL is managed by UT-Battelle, LLC, for the U. S. Department of Energy. This work is based upon experiments performed at the MARIA instrument operated by JCNS at the Heinz Maier-Leibnitz Zentrum (MLZ), Garching, Germany. The authors thank the Neutron Optics Group at the MLZ for providing measurement time at their Bruker D8 Discover reflectometer.

References

[1] B.J. Kirby, H.F. Belliveau, D.D. Belyea, P.A. Kienzle, A.J. Grutter, P. Riego, A. Berger, C.W. Miller, Spatial evolution of the ferromagnetic phase transition in an exchange graded film, Phys. Rev. Lett. 116 (2016) 047203, https://doi.org/10.1103/PhysRevLett.116.047203.

[2] J.M. Cowley, P.K. Larsen, P.J. Dobson, RHEED and Reflection Electron Imaging of Surfaces, Plenum Press, New York, 1988.

[3] W. Braun, Applied RHEED: Reflection High-Energy Electron Diffraction During Crystal Growth, Springer Berlin Heidelberg, 1999.

[4] J.A. Venables, G.D.T. Spiller, Nucleation and Growth of Thin Films, Springer US, Boston, MA, pp. 341–404. 10.1007/978-1-4684-4343-1_16.

[5] J.H. Haeni, C.D. Theis, D.G. Schlom, Rheed intensity oscillations for the stoichiometric growth of $SrTiO_3$ thin films by reactive molecular beam epitaxy, J. Electroceram. 4 (2) (2000) 385–391.

[6] J. Hemberger, A. Krimmel, T. Kurz, H.-A. Krug von Nidda, V.Y. Ivanov, A. A. Mukhin, A.M. Balbashov, A. Loidl, Structural, magnetic, and electrical properties of single-crystalline $La_{1-x}Sr_xMnO_3$ (0.4 & lt;x & lt;0.85), Phys. Rev. B 66 (2002) 094410, https://doi.org/10.1103/PhysRevB.66.094410.

[7] Y. Chen, D. Xu, K. Xu, N. Zhang, S. Liu, J. Zhao, Q. Luo, L.W. Snyman, J.W. Swart, Optoelectronic properties analysis of silicon light-emitting diode monolithically integrated in standard CMOS IC, Chin. Phys. B 28 (10) (2019) 107801, https://doi.org/10.1088/1674-1056/ab3e44.

[8] C. Adamo, X. Ke, P. Schiffer, A. Soukiassian, M. Warusawithana, L. Maritato, D. G. Schlom, Electrical and magnetic properties of $(SrMnO_3)_n/(LaMnO_3)_{2n}$ superlattices, Appl. Phys. Lett. 92 (11) (2008) 112508, https://doi.org/10.1063/1.2842421.

[9] Y.F. Nie, Y. Zhu, C.-H. Lee, L.F. Kourkoutis, J.A. Mundy, J. Junquera, P. Ghosez, D. J. Baek, S. Sung, X.X. Xi, K.M. Shen, D.A. Muller, D.G. Schlom, Atomically precise interfaces from non-stoichiometric deposition, Nat. Commun. 5 (1) (2014) 4530.

[10] C.-H. Lee, N.D. Orloff, T. Birol, Y. Zhu, V. Goian, E. Rocas, R. Haislmaier, E. Vlahos, J.A. Mundy, L.F. Kourkoutis, Y. Nie, M.D. Biegalski, J. Zhang, M. Bernhagen, N. A. Benedek, Y. Kim, J.D. Brock, R. Uecker, X.X. Xi, V. Gopalan, D. Nuzhnyy, S. Kamba, D.A. Muller, I. Takeuchi, J.C. Booth, C.J. Fennie, D.G. Schlom, Exploiting dimensionality and defect mitigation to create tunable microwave dielectrics, Nature 502 (7472) (2013) 532–536.

[11] D. Abou-Ras, B. Schaffer, M. Schaffer, S.S. Schmidt, R. Caballero, T. Unold, Direct insight into grain boundary reconstruction in Polycrystalline Cu(In,Ga)Se_2 with atomic resolution, Phys. Rev. Lett. 108 (7) (2012), https://doi.org/10.1103/physrevlett.108.075502.

[12] D. Mukherjee, N. Bingham, M. Hordagoda, M.-H. Phan, H. Srikanth, S. Witanachchi, P. Mukherjee, Influence of microstructure and interfacial strain on the magnetic properties of epitaxial $Mn_3O_4/La_{0.7}Sr_{0.3}MnO_3$ layered-composite thin films, J. Appl. Phys. 112 (8) (2020) 083910, https://doi.org/10.1063/1.4759237.

[13] D. Mukherjee, N. Bingham, M.-H. Phan, H. Srikanth, P. Mukherjee, S. Witanachchi, Ziz-zag interface and strain-influenced ferromagnetism in epitaxial $Mn_3O_4/La_{0.7}Sr_{0.3}MnO_3$ thin films grown on $SrTiO_3$ (100) substrates, J. Appl. Phys. 111 (7) (2012) 07D730, https://doi.org/10.1063/1.3680531.

[14] M. Kruth, D. Meertens, K. Tillmann, FEI helios NanoLab 460f1 FIB-SEM, J. Large-Scale Res. Facil. 2 (2016), https://doi.org/10.17815/jlsrf-2-105.

[15] M. Luysberg, M. Heggen, K. Tillmann, FEI tecnai g2 f20, J. Large-Scale Res. Facil. 2 (2016), https://doi.org/10.17815/jlsrf-2-138.

[16] M. Heggen, M. Luysberg, K. Tillmann, FEI titan 80-300 STEM, J. Large-Scale Res. Facil. 2 (2016), https://doi.org/10.17815/jlsrf-2-67.

[17] S. Mattauch, A. Koutsioubas, U. Rücker, D. Korolkov, V. Fracassi, J. Daemen, R. Schmitz, K. Bussmann, F. Suxdorf, M. Wagener, P. Kämmerling, H. Kleines, L. Fleischhauer-Fuß, M. Bednareck, V. Ossoviy, A. Nebel, P. Stronciwilk, S. Staringer, M. Gödel, A. Richter, H. Kusche, T. Kohnke, A. Ioffe, E. Babcock, Z. Salhi, T. Bruckel, The high-intensity reflectometer of the jülich centre for neutron science: MARIA, J. Appl. Crystallogr. 51 (3) (2018) 646–654, https://doi.org/10.1107/s1600576718006994.

[18] V. Lauter, H. Ambaye, R. Goyette, W.-T.H. Lee, A. Parizzi, Highlights from the magnetism reflectometer at the SNS, Physica B 404 (17) (2009) 2543–2546, https://doi.org/10.1016/j.physb.2009.06.021.

[19] H. Boschker, M. Huijben, A. Vailionis, J. Verbeeck, S. van Aert, M. Luysberg, S. Bals, G. van Tendeloo, E.P. Houwman, G. Koster, D.H.A. Blank, G. Rijnders, Optimized fabrication of high-quality $La_{0.67}Sr_{0.33}MnO_3$ thin films considering all essential characteristics, J. Phys. D 44 (20) (2011) 205001, https://doi.org/10.1088/0022-3727/44/20/205001.

[20] M. Björck, G. Andersson, GenX: an extensible x-ray reflectivity refinement program utilizing differential evolution, J. Appl. Crystallogr. 40 (6) (2007) 1174–1178, https://doi.org/10.1107/s0021889807045086.

[21] S. Gregory, Magnetic susceptibility of oxygen adsorbed on graphite, Phys. Rev. Lett. 40 (11) (1978) 723–725, https://doi.org/10.1103/physrevlett.40.723.

[22] MPMS Application Note 1014-210B: Oxygen Contamination; Quantum Design, 1997.

[23] B. Boucher, R. Buhl, M. Perrin, Magnetic structure of Mn_3O_4 by neutron diffraction, J. Appl. Phys. 42 (4) (1971) 1615–1617, https://doi.org/10.1063/1.1660364.

[24] K. Dwight, N. Menyuk, Magnetic properties of Mn_3O_4 and the canted spin problem, Phys. Rev. 119 (5) (1960) 1470–1479, https://doi.org/10.1103/physrev.119.1470.

[25] D. Shulyatev, S. Karabashev, A. Arsenov, Y. Mukovskii, S. Zverkov, Floating zone growth and properties of $La_{1-x}A_xMnO_3$ (A=Ca,Sr) single crystals, J. Cryst. Growth 237-239 (2002) 810–814, https://doi.org/10.1016/s0022-0248(01)02037-1.

[26] A. Balbashov, S. Karabashev, Y. Mukovskiy, S. Zverkov, Growth and giant magnetoresistance effect in $La_{1-x}Ca_xMnO_3$ and $La_{1-x}Sr_xMnO_3$ single crystals, J. Cryst. Growth 167 (1-2) (1996) 365–368, https://doi.org/10.1016/0022-0248(96)00184-4.

[27] D. Shulyatev, S. Karabashev, A. Arsenov, Y. Mukovskii, Growth and investigation of doped rare earth manganite single crystals, J. Cryst. Growth 198-199 (1999) 511–515, https://doi.org/10.1016/s0022-0248(98)01146-4.

[28] G. Rijnders. The initial growth of complex oxides: Study and Manipulation, University of Twente, 2001. Ph.D. thesis.

[29] Y. Ishii, H. Sato, A. Sawa, T. Yamada, H. Akoh, K. Endo, M. Kawasaki, Y. Tokura, Precipitate-free films of $La_{1-x}Sr_xMnO_3$ grown on the substrates with artificial step edges, Appl. Phys. Lett. 85 (17) (2004) 3800–3802, https://doi.org/10.1063/1.1807969.

[30] B. Vertruyen, R. Cloots, M. Ausloos, J.-F. Fagnard, P. Vanderbemden, Electrical transport and percolation in magnetoresistive manganite/insulating oxide composites: Case of $La_{0.7}Ca_{0.3}MnO_3/Mn_3O_4$, Physical Review B 75 (16) (2007), https://doi.org/10.1103/physrevb.75.165112.

[31] R.B. Comes, D.E. Perea, S.R. Spurgeon, Heterogeneous two-phase pillars in epitaxial $NiFe_2O_4$-$LaFeO_3$ nanocomposites, Adv. Mater. Interface. 4 (16) (2017) 1700396, https://doi.org/10.1002/admi.201700396.

[32] H. Zheng, Multiferroic $BaTiO_3$-$CoFe_2O_4$ nanostructures, Science 303 (5658) (2004) 661–663, https://doi.org/10.1126/science.1094207.

[33] S.R. Spurgeon, P.V. Sushko, A. Devaraj, Y. Du, T. Droubay, S.A. Chambers, Onset of phase separation in the double perovskite oxide La_2MnNiO_6, Phys. Rev. B 97 (2018) 134110, https://doi.org/10.1103/PhysRevB.97.134110.

[34] S.R. Spurgeon, Y. Du, T. Droubay, A. Devaraj, X. Sang, P. Longo, P. Yan, P. G. Kotula, V. Shutthanandan, M.E. Bowden, J.M. LeBeau, C. Wang, P.V. Sushko, S. A. Chambers, Competing pathways for nucleation of the double perovskite structure in the epitaxial synthesis of La_2MnNiO_6, Chem. Mater. 28 (11) (2016) 3814–3822, https://doi.org/10.1021/acs.chemmater.6b00829.